

# Warm Molecular Gas in M51: Mapping the Excitation Temperature and Mass of H<sub>2</sub> with the Spitzer Infrared Spectrograph

Gregory Brunner<sup>1,2</sup>

Department of Physics and Astronomy, Rice University,  
Houston, TX 77005

`gbrunner@rice.edu`

Kartik Sheth<sup>3</sup>, Lee Armus<sup>3</sup>

Spitzer Science Center, Caltech, Pasadena, CA 91125

Mark Wolfire<sup>4</sup>, Stuart Vogel<sup>4</sup>

Department of Astronomy, University of Maryland, College Park, MD 20741

Eva Schinnerer<sup>5</sup>

Max-Planck-Institut für Astronomie, Heidelberg, Germany

John-David Smith<sup>6</sup>

University of Arizona, Steward Observatory, Tucson, AZ 85721

Reginald Dufour<sup>1</sup>

Department of Physics and Astronomy, Rice University, Houston, TX 77005

George Helou<sup>3</sup>

Spitzer Science Center, Caltech, Pasadena, CA 91125

and

Daniel A. Dale<sup>7</sup>

Department of Physics and Astronomy, University of Wyoming, Laramie, WY 82071

Received \_\_\_\_\_; accepted \_\_\_\_\_

---

<sup>1</sup>Department of Physics and Astronomy, Rice University, Houston, TX 77005

<sup>2</sup>Visiting Graduate Student Fellow, Spitzer Science Center, Caltech, Pasadena, CA 91125

<sup>3</sup>Spitzer Science Center, Caltech, Pasadena, CA 91125

<sup>4</sup>Department of Astronomy, University of Maryland, College Park, MD 20741

<sup>5</sup>Max-Planck-Institut für Astronomie, Heidelberg, Germany

<sup>6</sup>University of Arizona, Steward Observatory, Tucson, AZ 85721

<sup>7</sup>Department of Physics and Astronomy, University of Wyoming, Laramie, WY 82071

## ABSTRACT

We have mapped the warm molecular gas traced by the  $\text{H}_2$  S(0) –  $\text{H}_2$  S(5) pure rotational mid-infrared emission lines over a radial strip across the nucleus and disk of M51 using the Infrared Spectrograph (IRS) on the *Spitzer Space Telescope*. The morphology of the molecular gas changes significantly between the different line maps. We obtained the  $\text{H}_2$  temperature and surface density distributions by assuming a two temperature model: a warm ( $T = 100 - 300$  K) phase using the low  $J$  (S(0) – S(2)) lines and a hot phase ( $T = 400 - 1000$  K) using the high  $J$  (S(2) – S(5)) lines. The coolest molecular gas temperatures are found within the spiral arms ( $T \sim 155$  K), while the warmest temperatures are found in the inter-arm regions ( $T > 800$  K). The warm gas surface density reaches a maximum of  $11.0 \text{ M}_\odot \text{ pc}^{-2}$  in the north-western spiral arm, whereas the hot gas surface density peaks at  $0.24 \text{ M}_\odot \text{ pc}^{-2}$  at the nucleus. The spatial offset between the peaks in the warm and hot phases indicates the different excitation mechanisms in the nucleus and in the spiral arms. The warm  $\text{H}_2$  is found in the dust lanes of M51, spatially offset from the brightest  $\text{H}\alpha$  regions. The warm  $\text{H}_2$  is generally spatially coincident with the colder ( $T \sim 10$  K) molecular gas traced by CO ( $J = 1 - 0$ ) emission indicating that the warm phase is excited in dense photodissociation regions (PDRs) within the spiral arms. In contrast, the hot  $\text{H}_2$  is most prominent in the nuclear region; here the hot  $\text{H}_2$  coincides with with [O IV]( $25.89 \mu\text{m}$ ) and X-ray emission, indicating that shocks and/or X-rays are responsible for exciting this phase.

*Subject headings:* galaxies: ISM — galaxies:  $\text{H}_2$  — galaxies: individual(M51)

## 1. Introduction

Star formation and galactic evolution are connected via the molecular gas in a galaxy. In the Milky Way, star formation occurs in molecular clouds, although not all clouds are actively forming stars. On a global, galactic scale, star formation may be triggered whenever the molecular gas surface density is enhanced, for example, by a spiral density wave (Vogel et al. 1988), by increased pressure or gas density in galactic nuclei (Young and Scoville 1991; Sheth et al. 2005), by hydrodynamic shocks along the leading edge of bars (Sheth et al. 2000; Sheth et al. 2002), and in the transition region at the ends of bars (Kenny and Lord 1991; Sheth et al. 2002). How does this star formation affect the surrounding molecular gas? How is it heated and what is the distribution of the gas temperatures? How does the mass of the warm and hot gas vary from region to region? We address these questions using spectral line maps from a radial strip across the grand-design spiral galaxy, M51.

M51 (the Whirlpool galaxy, NGC 5194) is a nearby, face-on spiral galaxy that is rich in molecular gas. Its proximity (assumed to be 8.2 Mpc (Tully 1988)), face-on orientation, and grand-design spiral morphology make it the ideal target for studies of the interstellar medium (ISM) across distinct dynamical, chemical, and physical environments in a galaxy. Studies of the molecular gas within M51 have revealed giant molecular associations (GMAs) along the spiral arms (Vogel et al. 1988; Rand and Kulkarni 1990; Aalto et al. 1999), a reservoir of molecular gas in the nucleus that is massive enough to fuel the AGN (Scoville et al. 1998), and spiral density wave triggered star-formation in molecular clouds (Vogel et al. 1988). In addition to being well-studied at millimeter and radio wavelengths, M51 has also been studied at X-ray, UV, optical, near-infrared, infrared, and submillimeter wavelengths (Palumbo et al. 1985; Terashima and Wilson 2001; Scoville et al. 2001; Calzetti et al. 2005; Matsushita et al. 2004).

In this paper we present maps of the  $\text{H}_2$  S(0) –  $\text{H}_2$  S(5) pure rotational mid-infrared line intensities over a strip across M51 created from *Spitzer Space Telescope* Infrared Spectrograph (IRS) spectral mapping mode observations. The mid-infrared  $\text{H}_2$  lines trace the warm ( $T = 100 - 1000$  K) phase of  $\text{H}_2$  and we use these lines to model the  $\text{H}_2$  excitation-temperature, mass (Rigopoulou et al. 2002; Higdon et al. 2006), and ortho-to-para ratio (Neufeld et al. 1998; Neufeld et al. 2006) across the M51 strips.<sup>1</sup> We use the inferred distributions to place constraints on the energy injection mechanisms (i.e. radiative heating, shocks, turbulence) that heat the warm molecular gas phase of the interstellar medium (ISM).

## 2. Observations and Data Reduction

### 2.1. Spectral Data

We mapped a radial strip across M51 using the short-low (SL;  $5 - 14.5 \mu\text{m}$ ) and long-low (LL;  $14 - 38 \mu\text{m}$ ) modules of the *Spitzer* IRS in spectral mapping mode (Houck et al. 2004). The radial strips were  $324'' \times 57''$  and  $295'' \times 51''$  in the SL and LL, respectively. Each slit position was mapped twice with half-slit spacings. In total, 1,412 spectra were taken in the SL and 100 were taken in the LL. Integration times for individual spectra were 14.6 s in both the SL and LL. Dedicated off source background observations were taken for the SL observations. Backgrounds for the LL observations were taken from outrigger data collected while the spacecraft was mapping in the adjacent module. Uncertainties in IRS fluxes are on the order of 25% (Smith et al. 2004). The astronomical observation requests (AORs)

---

<sup>1</sup>While we are always exploring the warm phase of  $\text{H}_2$ , in this paper we refer to a warm and a hot phase corresponding to temperatures of  $T = 100 - 300$  K and  $T = 400 - 1000$  K, respectively.

are available on SST’s Leopard and Spot (Project ID 200138, PI: K. Sheth).

The spectra were assembled from the basic calibration data (BCD) into spectral data cubes for each module using CUBISM (Kennicutt et al. 2003; Smith et al. 2004). Background subtraction and bad pixel removal were done within CUBISM. The individual BCDs were processed using the S14.0 version of the Spitzer Science Center (SSC) pipeline. In CUBISM, the SL and LL data cubes have  $1''.85$  and  $5''.08$  pixels, respectively. This pixel size is half the point spread function (PSF) at the red end of a given module. In principle, the PSF should vary with wavelength but since the PSF is undersampled at the blue end of the module, it is approximately constant across a given module. So the approximate resolution of the SL and LL modules is  $3''.7$  and  $10''.1$ , respectively.

We created continuum-subtracted line intensity maps of the  $\text{H}_2$  S(0) –  $\text{H}_2$  S(5) lines using a combination of PAHFIT (Smith et al. 2007) and our own code. PAHFIT is a spectral fitting routine that decomposes IRS low resolution spectra into broad PAH features, unresolved line emission, and grain continuum with the main advantage being that it allows one to recover the full line flux of any blended features. It also solves for the foreground dust emission and dereddens the emitted line intensities. Several  $\text{H}_2$  lines are blended:  $\text{H}_2$  S(1) with the  $17.0\ \mu\text{m}$  PAH complex,  $\text{H}_2$  S(2) with the  $12.0$  and  $12.6\ \mu\text{m}$  PAH complexes, and the  $\text{H}_2$  S(5) with the  $[\text{Ar II}](6.9\ \mu\text{m})$  line. We first concatenated SL1 and SL2, and LL1 and LL2 data cubes into two cubes, one for SL and one for LL. We smoothed each map in the cubes by a  $3 \times 3$  pixel box, conserving the flux, to increase the signal-to-noise ratio of the spectra. Then, for each pixel, we extracted a spectrum and ran PAHFIT to decompose it. We saved the location of the pixel on the sky along with the PAHFIT output (i.e. integrated line flux, line full width at half-max, line equivalent width, the uncertainty in the line flux, the fit to the entire spectrum and the fit to the continuum) for each spectrum and used this information to construct line flux maps for all of the mid-infrared features.

In addition to creating line maps, we created maps of line FWHM, line equivalent width, and uncertainty in the flux and data cubes of the fit to the entire spectrum, the fit to the continuum, a continuum subtracted data cube, and a residual data cube. In this paper we focus primarily on the  $\text{H}_2$  line maps.

## 2.2. Ancillary Data: CO ( $J = 1 - 0$ ), $\text{H}\alpha$ , and X-ray Observations

In this section we briefly discuss the ancillary data that we have used in order to understand  $\text{H}_2$  excitation in M51. We take note of the image resolutions for comparison to *Spitzer* IRS beam.

The BIMA (Berkely Illinois Maryland Array) CO ( $J = 1 - 0$ ) map was acquired as part of the BIMA Survey of Nearby Galaxies (SONG) (Regan et al. 2001; Helfer et al. 2003). At the distance of M51, the SONG beam ( $5''.8 \times 5''.1$ ) subtends  $220 \text{ pc} \times 190 \text{ pc}$ . The  $\text{H}\alpha$  + [N II] image of M51 was obtained from the *Spitzer Infrared Nearby Galaxies Survey* (SINGS) archive. The native pixel scale for the image is  $0''.3$  and the angular resolution is  $\sim 1''$ . X-ray emission from M51 was observed by the Advanced CCD Imaging Spectrometer (ACIS) on the *Chandra X-Ray Observatory* on 20 June 2000. The resolution of the image is  $\sim 1''$ . The X-ray image that we use has been presented and discussed in Terashima and Wilson et al. (2001).

## 3. Results

### 3.1. Morphology of $\text{H}_2$ Emission

We have detected and mapped  $\text{H}_2$  emission from the six lowest pure rotational  $\text{H}_2$  lines (Figure 1). The maps reveal remarkable differences in the distribution of the  $\text{H}_2$  emission

in M51.  $\text{H}_2$  S(0) emission is strongest in the northwest inner spiral arm peaking at an intensity of  $3.66 \times 10^{-18} \text{ W m}^{-2}$  and decreases by a factor of 2 in the nuclear region. In contrast, the  $\text{H}_2$  S(1) emission peaks in the nucleus of the galaxy at an intensity of  $1.03 \times 10^{-17} \text{ W m}^{-2}$  and has an extension of equal intensity towards the northwest inner spiral arm. In the spiral arm itself, the  $\text{H}_2$  S(0) peak is offset from the  $\text{H}_2$  S(1) emission by  $10''.2$  ( $\sim 380 \text{ pc}$ ). We find  $\text{H}_2$  S(0) and  $\text{H}_2$  S(1) emission as far as  $5 - 6 \text{ kpc}$  from the nucleus of the galaxy. In the outer spiral arms, the  $\text{H}_2$  S(0) intensity is a factor of 2 times lower than in the inner northwest spiral arm and the  $\text{H}_2$  S(1) intensity is a factor of 5 times lower than in the nucleus.

The  $\text{H}_2$  S(2) –  $\text{H}_2$  S(5) maps show different molecular gas morphology within M51 through each  $\text{H}_2$  line. The strongest  $\text{H}_2$  S(2) emission is from the nucleus at  $2.21 \times 10^{-18} \text{ W m}^{-2}$ . We also see bright  $\text{H}_2$  S(2) emission from the inner northwest spiral arm at half the intensity of the nuclear peak. The  $\text{H}_2$  S(3) peak at the nucleus is  $1.35 \times 10^{-17} \text{ W m}^{-2}$ , a factor of  $\sim 6$  greater than the  $\text{H}_2$  S(2) nuclear peak. There is also a linear bar-like structure in  $\text{H}_2$  S(3) emission across the nucleus of the galaxy at a  $\text{PA} \sim -10^\circ$ . The emission peaks in the  $\text{H}_2$  S(2) and  $\text{H}_2$  S(3) maps are not spatially coincident. For instance, in the inner spiral arm there is a  $\text{H}_2$  S(2) peak coincident with the CO peak whereas the  $\text{H}_2$  S(3) peaks further down the spiral arm. Offsets like these suggest that there may be variations in the excitation temperature from region to region within a galaxy, and even within a spiral arm.

The  $\text{H}_2$  S(4) and  $\text{H}_2$  S(5) lines are brightest at the nucleus with intensities of 3.05 and  $8.04 \times 10^{-18} \text{ W m}^{-2}$ , respectively. The  $\text{H}_2$  S(4) line shows emission in the nucleus and in the spiral arm to the west. In the spiral arm to the west of the nucleus, the  $\text{H}_2$  S(4) intensity is  $2.11 \times 10^{-18} \text{ W m}^{-2}$ . This is notable because the spiral arm to the southwest of the nucleus is very bright in CO and studies have revealed very high molecular gas column densities in the southwest inner spiral arm (Lord and Young 1990).  $\text{H}_2$  S(5) emission is



asymmetric in the nucleus and mimics the morphology of the H<sub>2</sub> S(3) line with extended emission to the north of the nucleus. The differences in the morphology of H<sub>2</sub> emission are indicative of changes in the H<sub>2</sub> excitation temperature across the galaxy, which we discuss in the next section.

### 3.2. Mapping H<sub>2</sub> Excitation Temperature and Surface Density across M51

#### 3.2.1. Modeling H<sub>2</sub> Excitation Temperature and Surface Density

The pure rotational lines of molecular hydrogen provide a powerful probe of the conditions of the ISM by placing constraints on the energy injection that excites H<sub>2</sub> (Neufeld et al. 2006). Following Rigopoulou et al. (2002) and Higdon et al. (2006) we modeled the H<sub>2</sub> temperature and mass across M51.

First, we smoothed the H<sub>2</sub> S(1) – H<sub>2</sub> S(5) maps to the resolution of the H<sub>2</sub> S(0) map. The maps were then interpolated to the same spatial grid. Excitation diagrams across the strip were derived from the Boltzman equation using the formulation of Rigopoulou et al. (2002),

$$N_i/N = (g(i)/Z(T_{\text{ex}}))\exp(-T_i/T_{\text{ex}}) \quad (1)$$

where  $g(i)$  is the statistical weight of state  $i$ ,  $Z(T_{\text{ex}})$  is the partition function,  $T_i$  is the energy level of a given state, and  $T_{\text{ex}}$  is the excitation temperature.  $N$  and  $N_i$  are the total column density and the column density of a given state  $i$  and  $N_i$  is determined directly from the measured extinction-corrected flux by

$$N_i = 4\pi \times \text{flux}(i)/(\Omega A(i)h\nu(i)) \quad (2)$$

where  $A(i)$  is the Einstein  $A$ -coefficient,  $\nu(i)$  is the frequency of state  $i$ ,  $\Omega$  is the solid angle of the beam, and  $h$  is Planck’s constant. Table 1 lists the values for the wavelength,

rotational state, Einstein  $A$ -coefficient, energy, and statistical weight of the pure rotational levels of  $\text{H}_2$ .

Figure 2 shows excitation diagrams from three different regions across the M51 strip. The three regions are marked on the  $\text{H}_2$  surface density maps in Figure 3. In the nuclear region (Region 2) the ortho and para levels appear to lie along the same curve indicating an ortho-to-para ratio (OPR) of 3; the excitation diagrams do not exhibit the “zigzag” characteristic of a non-equilibrium  $\text{H}_2$  OPR (Neufeld et al. 1998; Fuente et al. 1999). In the southeast and northwest spiral arms (Regions 1 and 3, respectively) the lower  $J$  ( $\text{H}_2$  S(0) -  $\text{H}_2$  S(3)) levels exhibit an OPR of 3. The  $\text{H}_2$  S(4) measurement shows significant scatter in the excitation diagrams outside of the nuclear region of M51. This would indicate that the OPR is less than 3, however, due to the low signal-to-noise ratio of the  $\text{H}_2$  S(4) map, we do not believe that the OPR determined from the  $\text{H}_2$  S(4) intensity reflects the OPR of the warm  $\text{H}_2$ .

In order to derive temperature and surface density distributions we assume a two temperature model for the  $\text{H}_2$ . To determine the hot ( $T = 400 - 1000$  K) phase temperature, we do a least squares fit to the  $\text{H}_2$  S(2) –  $\text{H}_2$  S(5) column densities in the excitation diagram at every pixel in our maps. We then subtract the contribution of hot phase from the lower  $J$  lines and do a least squares fit to the column densities of  $\text{H}_2$  S(0) –  $\text{H}_2$  S(2) lines at every pixel in our maps to determine the temperature distribution of the warm ( $T = 100 - 300$  K) phase. The warm and hot phase surface density distributions are derived from the column densities of the  $\text{H}_2$  S(0) and  $\text{H}_2$  S(3) lines, respectively. The column densities are easily converted to mass surface density by determining the mass of the warm and hot  $\text{H}_2$  within every pixel.

### 3.2.2. Warm and Hot $H_2$ Excitation Temperature and Surface Density Distributions

Figure 3 presents the warm (*left*) and hot (*right*)  $H_2$  surface density distributions across the M51 strip.<sup>2</sup> The highest gas surface density for the warm  $H_2$  phase is in the inner northwest spiral arm at  $11 \text{ M}_\odot \text{ pc}^{-2}$ . The gas surface density in the outer northwest and southeast spiral arms is maximum at the center of the spiral arms at  $3.5 \text{ M}_\odot \text{ pc}^{-2}$  and  $1.0 \text{ M}_\odot \text{ pc}^{-2}$  respectively. The hot phase surface density is highest in the nucleus and interior to the inner spiral arm at  $0.24 \text{ M}_\odot \text{ pc}^{-2}$ . The gas surface density of the hot phase in the spiral arms is 3 – 5 times lower than that of the nuclear region.

Figures 4 and 5 show the distribution of the warm and hot  $H_2$  temperatures (in grayscale) with the contours of the  $H_2$  gas surface density overlaid. In both cases we see that the temperature and surface density are inversely correlated with the hottest temperatures corresponding to regions of lowest surface density. For both the warm and hot phases, we see the temperature is higher in the inter-arm regions than in the spiral arms. We believe that this is real and does not result from lower signal-to-noise in the inter-arm regions. A lower signal-to-noise ratio would increase the slope of the line in the least squares fit to the warm and hot  $H_2$  excitation diagrams and result in a lower temperature.

Figure 6 compares the warm (in grayscale) and hot (in contours)  $H_2$  surface density distributions. The warm  $H_2$  mass distribution peaks in the northwest inner spiral arm and the hot  $H_2$  mass distribution peaks in the nucleus and in the region interior to the northwest spiral arm. The warm-to-hot  $H_2$  mass ratio is not constant across the galaxy but is lowest ( $\sim 12$ ) in the nucleus of the galaxy and increases to 170 and 136 in the southeast and northwest spiral arms, respectively.

---

<sup>2</sup>Note that the non-rectangular shape of the strip is due to the offset between the SL and LL strips.

## 4. Discussion

### 4.1. The Distribution of the Warm and Hot H<sub>2</sub> in M51

Previous studies have used aperture-averages over entire galactic nuclei to derive the physical conditions of the molecular gas (Rigopoulou et al. 2002; Higdon et al. 2006; Roussel et al. 2007). In M51, Roussel et al. (2007) finds that within the central 330 arcsec<sup>2</sup> ( $4.61 \times 10^5$  pc<sup>2</sup>), the warm H<sub>2</sub> phase has a temperature of 180 K and a surface density of  $3.16 \text{ M}_\odot \text{ pc}^{-2}$  (a total mass of  $M_{\text{warm}} = 1.46 \times 10^6 \text{ M}_\odot$ ). Roussel et al. (2007) has also measured the temperature of the hot phase (though they do not measure the mass in the hot phase) and find a hot H<sub>2</sub> temperature of 521 K.

Having spatially resolved spectra over a strip across M51, we can understand the behavior of the warm and hot H<sub>2</sub> phases on smaller scales. In the nuclear region of M51 we see that the warm phase temperature peaks at 192 K and decreases radially into the inner spiral arms. The warm H<sub>2</sub> surface density at the nucleus is  $4.39 \text{ M}_\odot \text{ pc}^{-2}$  and decreases within a 0.5 kpc radius surrounding the nucleus. To check the consistency of our results against those of Roussel et al. (2007), we averaged the warm phase temperature over a similar 412 arcsec<sup>2</sup> ( $5.76 \times 10^2 \text{ pc}^2$ ) aperture and found that the warm phase temperature and surface density are 186 K and  $2.82 \text{ M}_\odot \text{ pc}^{-2}$ , respectively. These results suggests that previous studies of the warm H<sub>2</sub> temperature and mass were biased by the large extraction apertures and the temperature and mass reflect an average value rather than a maximum value.

The warm-to-hot H<sub>2</sub> surface density ratio varies across M51 indicating that the heating mechanism for the warm and hot H<sub>2</sub> phases differ. The most obvious excitation mechanism for the molecular gas is star-formation or nuclear activity. The former can be traced with H $\alpha$  emission (Scoville et al. 2001) and the latter using X-rays or the [O IV](25.89  $\mu\text{m}$ ) line

(Schearer and Stasinska 1999; Smith et al. 2004). We are also interested in how the warm molecular gas is distributed relative to the cold ( $T \sim 10$  K) molecular gas in giant molecular clouds, so we compare the  $H_2$  maps to CO data from BIMA SONG.

#### 4.2. Distinguishing the $H_2$ Excitation Mechanisms

Owing to a dissociation energy of 4.5 eV,  $H_2$  formation generally does not occur within a PDR until the radiation field becomes sufficiently weak. Kaufman et al. (2006) show that within galaxies, where the telescope beam size is generally kiloparsecs across,  $H_2$  emission could serve to probe the surface layers of dense molecular clouds. In Figure 7, we compare the warm (*left*) and hot  $H_2$  (*right*) mass distributions to the cold ( $T \sim 10$  K) phase of  $H_2$  traced by CO ( $J = 1 - 0$ ) emission. The warm and hot  $H_2$  phases appear to trace the bright CO emission in the northwest and southeast spiral arms. Comparison of CO to the individual  $H_2$  S(0) –  $H_2$  S(3) line intensity maps in Figure 8 also shows that the  $H_2$  in the spiral arms traces the bright CO emission. The most striking result is that in the inner spiral arms, we see that the CO is offset toward the nucleus from the warm  $H_2$  mass. The offset between the peaks in CO and warm  $H_2$  mass is  $7''.2$  in the northwest spiral arms and  $5''$  in the southeast spiral arms. We believe that these offsets are real with one possible explanation being that the  $H_2$  is tracing the regions of active star-formation within the giant molecular associations. In the nucleus of M51 the hot  $H_2$  density is highest, though there is very little cold  $H_2$  in comparison to the spiral arms.

Scoville et al. (2001) used  $H\alpha$  and  $P\alpha$  imagery to identify and characterize over 1,350 H II regions in M51. In Figure 9, we compare the warm (*left*) and hot (*right*)  $H_2$  mass distributions to  $H\alpha$  emission. In general, the warm and hot  $H_2$  concentrations are not cospatial with the brightest  $H\alpha$  emission regions in the spiral arms with the one exception being that the warm  $H_2$  mass in the inner spiral arms appears to trace the  $H\alpha$  emission.

The warm  $\text{H}_2$  mass contours show that local peaks in  $\text{H}_2$  mass are found within the dust lanes. An example of this is in the northwest spiral arms where we see the  $\text{H}_2$  mass offset from the  $\text{H}\alpha$  spiral arms with local peaks being found in the dust lanes. In Figure 10, we compare the  $\text{H}_2$  S(0) –  $\text{H}_2$  S(3) line intensity maps to  $\text{H}\alpha$  emission. Comparison of the  $\text{H}_2$  S(0) map to  $\text{H}\alpha$  reveals that the strongest  $\text{H}_2$  emission in the northwest and southeast inner spiral arms is coincident with  $\text{H}\alpha$  emission; however, the other  $\text{H}_2$  S(0) spiral arms show the strongest emission in the dust lanes, offset from the  $\text{H}\alpha$  spiral arms. The largest offsets are seen in the southeast spiral arm where the  $\text{H}_2$  S(0) emission is offset from the  $\text{H}\alpha$  spiral arm by  $\sim 15''$  (560 pc).  $\text{H}_2$  S(1) emission appears to follow the dust lanes and the  $\text{H}_2$  S(1) intensity subsides into the  $\text{H}\alpha$  spiral arms.  $\text{H}_2$  S(2) and  $\text{H}_2$  S(3) emission is also found in the dust lanes; however, there are instances (such as in the southeast spiral arm) where the  $\text{H}_2$  emission appear to be found straddling the dust lane and  $\text{H}\alpha$  spiral arm.

The [O IV](25.89  $\mu\text{m}$ ) line can be excited in shocks (Scheerer and Stasinska 1999), the stellar winds of massive Wolf-Rayet stars (Lutz et al. 1998), or by an active galactic nucleus (AGN)(Smith et al. 2004). Though the [O IV] line is blended with the [Fe II](25.99  $\mu\text{m}$ ) line in *Spitzer* IRS low resolution spectra, PAHFIT can deblend the two lines and in mapping the  $\text{H}_2$  S(0) and  $\text{H}_2$  S(1) lines in the LL data cubes we also mapped the [O IV] line. In Figure 11, we compare the [O IV] intensity to the warm (*left*) and hot (*right*)  $\text{H}_2$  distributions. The [O IV] emission is brightest in the nuclear region at  $8.75 \times 10^{-18} \text{ W m}^{-2}$  and the peak is coincident with the nuclear peak in the mass of the hot  $\text{H}_2$ . [O IV] emission subsides from the nucleus to the inner spiral arm by 50 %. We resolve weaker [O IV] emission within the warm and hot  $\text{H}_2$  spiral arms. The [O IV] intensity in the spiral arms is a factor of  $\sim 6$  lower in the spiral arms than the peak intensity found in the nucleus. The [O IV] emission within the nuclear region of M51 is likely due to the weak Seyfert II nucleus (Ford et al. 1985) and is possibly associated with shocked gas from the outflows of the AGN. The peak of the [O IV] emission coincides with the nuclear peak in

hot  $\text{H}_2$  mass indicating that the hot  $\text{H}_2$  phase in the nuclear region of the galaxy is AGN or shock heated. In the nuclear region we observe a factor of 12 times greater warm  $\text{H}_2$  mass. The warm  $\text{H}_2$  mass is much greater within the spiral arms than within the nucleus and the warm-to-hot mass ratio is lowest in the nuclear region where the  $[\text{O IV}]$  intensity is greatest. In the nuclear region, shocks appear to be a more efficient means to excite the hot  $\text{H}_2$  phase than the warm  $\text{H}_2$  phase.

M51 has been extensively studied in X-rays by ASCA (Terashima et al. 1998), Newton XMM (Dewangan et al. 2005), and the Chandra X-ray Observatory (Terashima and Wilson 2001). Terashima and Wilson (2001) have studied X-rays in nuclear region of M51 and they observe X-ray emission from the nucleus, the extranuclear cloud (XNC, to the south of the nucleus), and the northern loop. A radio jet that is believed to be shock heating the ISM has been observed emanating from the south of the nucleus towards the XNC in 6 cm imagery (Crane and van der Hulst 1992). In Figure 12, we compare the smoothed 0.5 - 10 keV band X-ray image to the warm (*left*) and hot (*right*)  $\text{H}_2$  mass distributions. The 0.5 - 10 keV band has been smoothed to the resolution of the warm and hot  $\text{H}_2$  mass distributions and the nucleus, XNC, and northern loop are indistinguishable in the smoothed image. X-ray emission is most intense from the nucleus and decreases into the northwest spiral arm that contains the greatest  $\text{H}_2$  mass. There appears to be very little connection between the 0.5 - 10 keV X-ray band and the warm  $\text{H}_2$  mass distribution. The peak in X-ray emission is coincident with the hot  $\text{H}_2$  mass peak. The most intense 0.5 - 10 keV X-ray emission originates from the nucleus and is oriented north-to-south, similar to the  $[\text{O IV}](25.89 \mu\text{m})$  emission. The peak in X-ray emission is located within the peak in hot  $\text{H}_2$  mass suggesting that X-rays play an important role in exciting the hot  $\text{H}_2$  phase. While there is a correlation between X-ray emission and the hot  $\text{H}_2$  phase,  $\text{H}_2$  excitation by X-rays cannot be distinguished from  $\text{H}_2$  excitation by shocks. In Figure 13, we compare the X-ray surface brightness to the  $\text{H}_2 \text{ S}(2) - \text{H}_2 \text{ S}(5)$  maps and

find that the nuclear H<sub>2</sub> emission appears to be correlated with the X-ray source.

## 5. Conclusions

We have spectrally mapped a strip across M51 using the *Spitzer* IRS low resolution modules. We used the spatially resolved spectra to map H<sub>2</sub> S(0) – H<sub>2</sub> S(5) line intensities across the strip. We find:

1. The morphology of H<sub>2</sub> emission in M51 varies with H<sub>2</sub> rotational level. H<sub>2</sub> S(0) emission is strongest in the spiral arms of the galaxy while the higher  $J$  transitions show the strongest emission towards the nucleus. The H<sub>2</sub> S(1) intensity is strongest in the nuclear region and is offset from the peak in H<sub>2</sub> S(0) intensity in the inner northwest spiral arm by 10''2. The H<sub>2</sub> S(2) and H<sub>2</sub> S(3) maps show H<sub>2</sub> emission in the nucleus, spiral arms, and inter-arm regions of M51 and bar structure aligned north-to-south is apparent in H<sub>2</sub> S(3) emission. H<sub>2</sub> S(4) and H<sub>2</sub> S(5) emission is resolved in the nuclear region of M51.
2. The different morphologies of H<sub>2</sub> emission in M51 indicate significant spatial variations in H<sub>2</sub> temperature and surface density. Excitation diagrams reveal that the H<sub>2</sub> exists in a range of temperatures across the galaxy. Using the low  $J$  lines to trace the warm (T = 100 – 300 K) H<sub>2</sub>, we find that the warm H<sub>2</sub> temperature is highest in the nuclear region at 192 K and the warm H<sub>2</sub> surface density peaks in the northwest inner spiral arm at 11 M<sub>⊙</sub> pc<sup>-2</sup>. Using the higher  $J$  lines to trace the hot (T = 400 – 1000 K) H<sub>2</sub>, we find that the hot H<sub>2</sub> temperature is lowest in the inner spiral arms (500 – 550 K) and increases to ~ 600 K in the nucleus where the largest hot H<sub>2</sub> surface density is found to be 0.24 M<sub>⊙</sub> pc<sup>-2</sup>.
3. The warm and the hot H<sub>2</sub> surface density distributions are not cospatial and the



warm-to-hot surface density ratio varies across M51. The hot  $\text{H}_2$  surface density distribution shows two peaks, one in the nucleus of M51 and one located interior to the northwest inner spiral arm of M51. The warm  $\text{H}_2$  surface density distribution peaks in the northwest spiral arm and is offset from the hot mass peak by  $11''.4$ . The warm-to-hot  $\text{H}_2$  ratio varies across the galaxy with the ratio being  $\sim 15$  in the nucleus and increasing to  $> 100$  in the spiral arms. Variations in the warm-to-hot  $\text{H}_2$  ratio and differences in the morphology of the  $\text{H}_2$  emission across M51 indicate that the primary excitation mechanism differs for the warm and hot  $\text{H}_2$  phases as a function of location within the galaxy.

4. The warm  $\text{H}_2$  traces the cold ( $T \sim 10$  K)  $\text{H}_2$  in the spiral arms of M51 indicating that the warm phase is associated with the surface layers of dense molecular clouds. The  $\text{H}_2$  S(0) –  $\text{H}_2$  S(3) contours trace the CO; however, within the spiral arms, the peaks in  $\text{H}_2$  can be offset from the peaks in CO intensity. In the nucleus, the  $\text{H}_2$  S(1) –  $\text{H}_2$  S(3) lines are brightest and the CO intensity is a factor of  $\sim 2.5$  weaker than in the spiral arms suggesting that  $\text{H}_2$  emission from the higher  $J$  lines is excited by shocks of X-rays.

5. Comparing the distributions of  $\text{H}_2$  to  $\text{H}\alpha$  reveals that the warm and hot  $\text{H}_2$  is found in the dust lanes rather than at or around the  $\text{H}\alpha$  emission regions with the one exception being that the warm  $\text{H}_2$  in the inner spiral arms is coincident with bright  $\text{H}\alpha$  emission.

6. The peaks in  $[\text{O IV}](25.89 \mu\text{m})$  intensity and X-ray intensity are both coincident with the peak in hot  $\text{H}_2$  surface density in the nucleus of M51 suggesting that the hot  $\text{H}_2$  in the nucleus is primarily excited by the AGN, shocks (possibly associated with the AGN), or X-rays associated with the AGN. The spatial distributions of the  $[\text{O IV}]$  emission and X-ray surface brightness are very similar preventing the characterization of the primary excitation

mechanism (shocks or X-rays) of the hot  $\text{H}_2$  phase.

The author graciously acknowledges the Spitzer Science Center Spitzer Visiting Graduate Student Fellowship program and committee for providing support for this research. The author would like to specifically acknowledge the program coordinators, Phil Appleton and Alberto Noriega-Crepso. Partial support for the completion and preparation for publication of this study by the author was provided by AURA grant GO10822.1 to Rice University.

*Facilities:* Spitzer Science Center (SSC), Spitzer Space Telescope (SST), Berkeley-Illinois-Maryland Array (BIMA).

## REFERENCES

- Aalto, S., Huttemeister, S., Scoville, N.Z., and Thaddeus, P., 1999, *AJ*, 522, 165
- Calzetti, D. et al., 2005, *ApJ*, 633, 871
- Crane, P.C. and van der Hulst, J.M., 1992, *AJ*, 103, 1146
- Dewangn, G.C., Griffiths, R.E., Choudhury, M., Miyaji, T., and Schurch, N.J., 2005, *ApJ*, 635, 198
- Ford, H.C., Crane, P.C., Jacoby, G.H., Lawrie, D.G., and van der Hulst, J.M., 1985, *ApJ*, 293, 132
- Fuente, A., Martín-Pintado, J., Rodríguez-Fernández, N.J., Rodríguez-Franco, A., de Vicente, P., and Kunze, D., 1999, *ApJ*, 518, L45
- Helfer, T.T., Thornley, M.D., Regan, M.W., Wong, T., Sheth, K., Vogel, S.N., Blitz, L., and Bock, D.C.J., 2003, *ApJS*, 145, 259
- Higdon, S.J.U., Armus, L., Higdon, J.L., Soifer, B.T., and Spoon, H.W.W., 2006, *ApJ*, 648, 323
- Houck, J.R. et al., 2004, *ApJS*, 145, 18
- Kaufman, M.J., Wolfire, M.G., and Hollenbach, D.J., 2006, *ApJ*, 644, 283
- Lord, S.D. and Young, J.S., 1990, *ApJ*, 356, 135
- Lutz, D., Kunze, D., Spoon, H.W.W., and Thornley, M.D., 1998, *A&A*, 333, L75
- Kennicutt, R.C. et al., 2003, *PASP*, 115, 928
- Kenny, J.D.P. and Lord, S.D., 1991, *ApJ*, 381, 118

- Matsushita, S. et al., 2004, *ApJ*, 616, L55
- Neufeld, D.A., Melnick, G.J., and Harwit, M., 1998, *ApJ*, 506, L75
- Neufeld, D.A., Melnick, G.J., Sonnentrucker, P., Bergin, E.A., Green, J.D., Kim, K.H.,  
Watson, D.M., Forrest, W.J., and Pipher, J.L., 2006, *ApJ*, 649, 816
- Palumbo, G.G.C., Fabbiano, G., Fransson, C., and Trinchieri, G., 1985, *ApJ*, 298, 259
- Rand, R.J. and Kulkarni, S.R., 1990, *ApJ*, 349, L43
- Regan, M.W., Thornley, M.D., Helfer, T.T., Sheth, K., Wong, T., Vogel, S.N., Blitz, L.,  
and Bock, D.C.J., 2001, *ApJ*, 561, 218
- Rigopoulou, D., Kunze, D., Lutz, D., Genzel, R., and Moorwood, A.F.M., 2002, *A&A*, 389,  
374
- Roussel, H. et al., 2007, in press
- Schaerer, D. and Stasinska, G., 1999, *A&A*, 345, L17
- Scoville, N.Z. and Young, J.S., 1983, *AJ*, 265, 148
- Scoville, N.Z., Yun, M.S., Armus, L., and Ford, H., 1998, *ApJ*, 493, L63
- Scoville, N.Z., Polletta, M., Ewald, S., Stolovy, S.R., Thompson, R., and Rieke, M., 2001,  
*AJ*, 122, 3017
- Sheth, K., Regan, M.W., Vogel, S.N., and Teuben, P.J., 2000, *ApJ*, 532, 221
- Sheth, K., Vogel, S.N., Regan, M.W., Teuben, P.J., Harris, A.I., and Thornley, M.D., 2002,  
*AJ*, 124, 2581
- Sheth, K., Vogel, S.N., Regan, M.W., Thornley, M.D., and Teuben, P.J., 2005, *ApJ*, 632,  
217

SINGS: The Spitzer Infrared Nearby Galaxies Fourth Data Delivery, May 2006.

Smith, J.D.T. et al., 2004, ApJS, 154, 199

Smith, J.D.T. et al., 2007, ApJ, 656, 770

Terashima, Y., Ptak, A., Fujimoto, M.I., Kunieda, H., Makishima, K., and Sherlemitsos, P.J., 1998, ApJ, 496, 210

Terashima, Y. and Wilson, A.S., 2001, ApJ, 560, 139

Tully, R.B. 1988, Nearby Galaxies catalog (Cambridge:Cambridge University Press)

Vogel, S.N., Kulkarni, S.R., and Scoville, S.Z., 1988, Nature, 334, 402

Young, J.S. and Devereux, N.A., 1991, ApJ, 373, 414

Young, J.S. and Scoville, N.Z., 1991, ARA&A, 29, 581

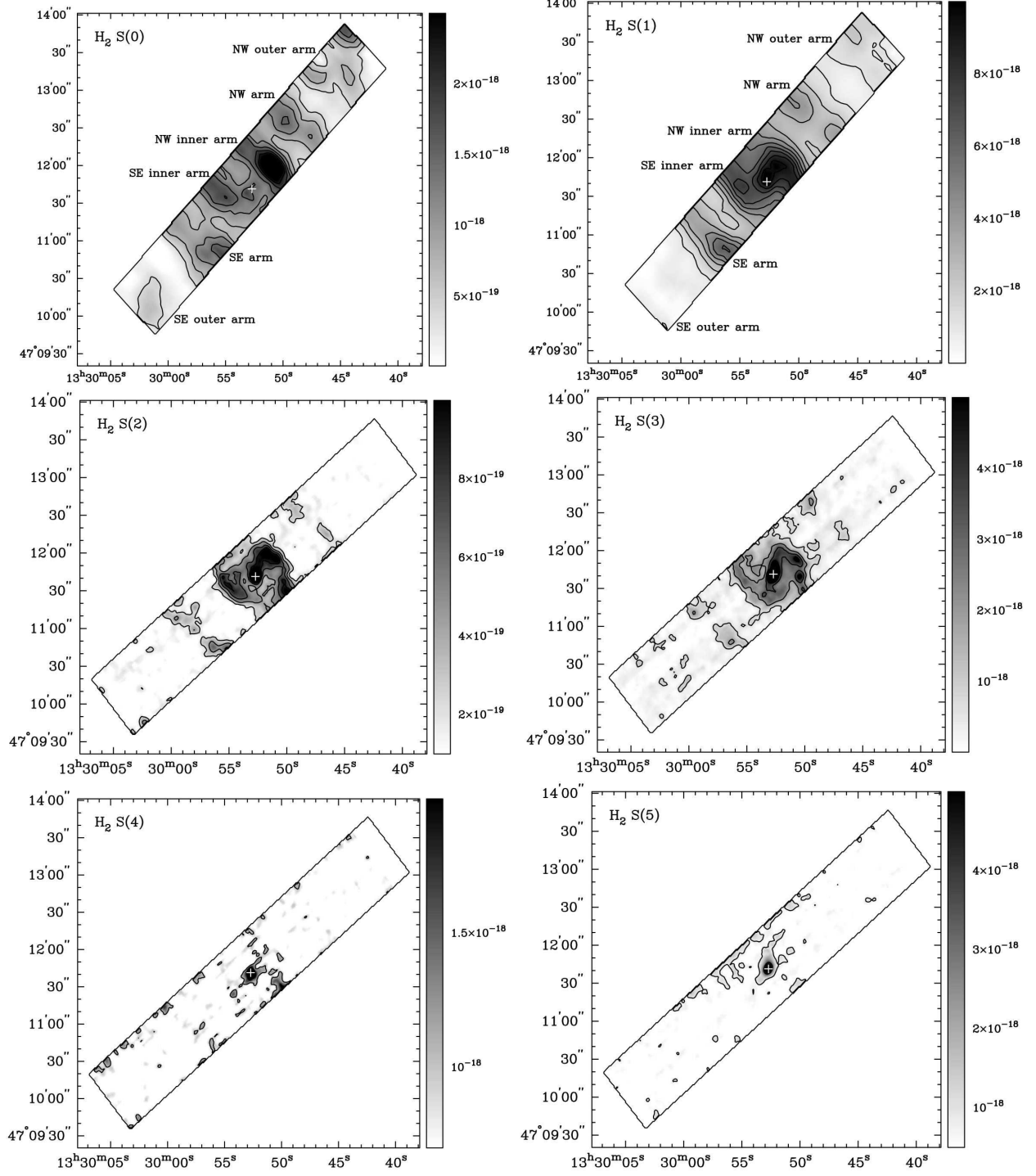


Fig. 1.— Maps of the H<sub>2</sub> S(0) (*top left*), H<sub>2</sub> S(1) (*top right*), H<sub>2</sub> S(2) (*middle left*), H<sub>2</sub> S(3) (*middle right*), H<sub>2</sub> S(4) (*bottom left*), and H<sub>2</sub> S(5) (*bottom right*) intensity across the SL and LL strips that we mapped with the Spitzer IRS. The H<sub>2</sub> S(0) and H<sub>2</sub> S(1) maps are created from the LL data cubes. The H<sub>2</sub> S(2), H<sub>2</sub> S(3), H<sub>2</sub> S(4), and H<sub>2</sub> S(5) maps are created from the SL data cube. The grayscale is in units of W m<sup>-2</sup>. Contour levels are at  $2.9 \times 10^{-18}$ ,  $2.2 \times 10^{-18}$ ,  $1.8 \times 10^{-18}$ ,  $1.5 \times 10^{-18}$ ,  $1.1 \times 10^{-18}$ ,  $7.3 \times 10^{-19}$ , and  $3.7 \times 10^{-19}$  W m<sup>-2</sup> for H<sub>2</sub> S(0);  $9.6 \times 10^{-18}$ ,  $8.6 \times 10^{-18}$ ,  $7.5 \times 10^{-18}$ ,  $6.4 \times 10^{-18}$ ,  $5.4 \times 10^{-18}$ ,  $4.3 \times 10^{-18}$ ,  $3.2 \times 10^{-18}$ ,  $2.1 \times 10^{-18}$  and  $1.1 \times 10^{-18}$  W m<sup>-2</sup> for H<sub>2</sub> S(1);  $1.1 \times 10^{-18}$ ,  $8.9 \times 10^{-19}$ ,  $6.7 \times 10^{-19}$ ,  $4.4 \times 10^{-19}$ , and  $2.2 \times 10^{-19}$  W m<sup>-2</sup> for H<sub>2</sub> S(2);  $1.21 \times 10^{-17}$ ,  $9.4 \times 10^{-18}$ ,  $6.7 \times 10^{-18}$ ,  $4.0 \times 10^{-18}$ , and  $1.3 \times 10^{-18}$  W m<sup>-2</sup> for H<sub>2</sub> S(3);  $2.0 \times 10^{-18}$  and  $1.0 \times 10^{-18}$  W m<sup>-2</sup> for H<sub>2</sub> S(4);  $7.3 \times 10^{-18}$ ,  $4.0 \times 10^{-18}$ , and  $8.0 \times 10^{-19}$  W m<sup>-2</sup> for H<sub>2</sub> S(5). The vertical axis is the right ascension and the horizontal axis is the declination. In all of the maps, north is up, east is to the left, and the cross denotes the nucleus of the galaxy. The different spiral arm regions are labeled on the H<sub>2</sub> S(0) and H<sub>2</sub> S(1) maps in order to aid in discussing the molecular gas morphologies. The box around the intensity maps represents the SL or LL strip that we mapped.

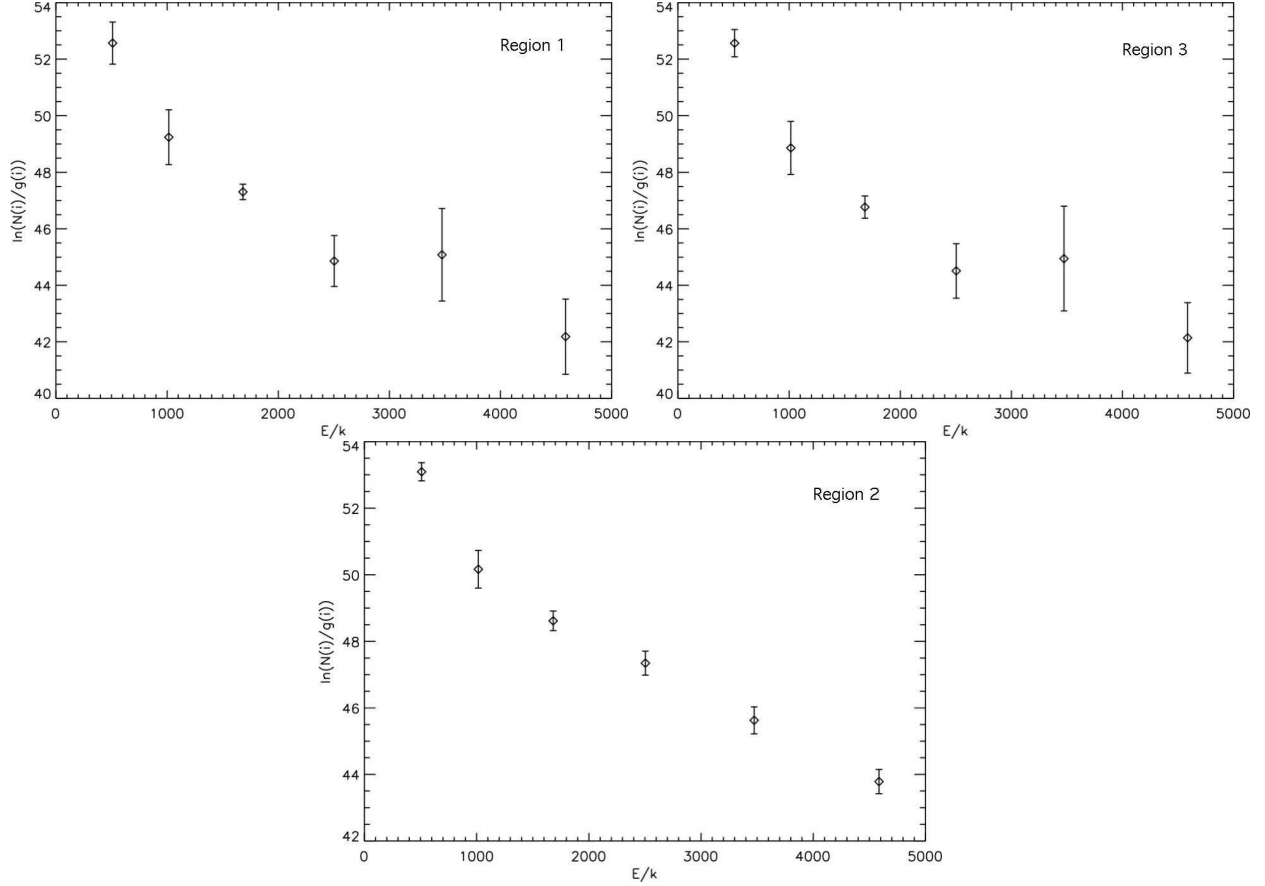


Fig. 2.— Excitation diagrams taken from 3 different single pixel regions along the M51 strip. The top two excitation diagrams (Regions 1 and 3) are taken from pixels at (RA, Dec) of (202.45, 47.21) and (202.49, 47.18) within the southeast and northwest spiral arms, respectively. The excitation diagram at the bottom (Region 2) is taken from from a pixel at (RA, Dec) of (202.47, 47.19) in the nuclear region. The different regions are marked on the  $H_2$  surface density maps (Figure 3).



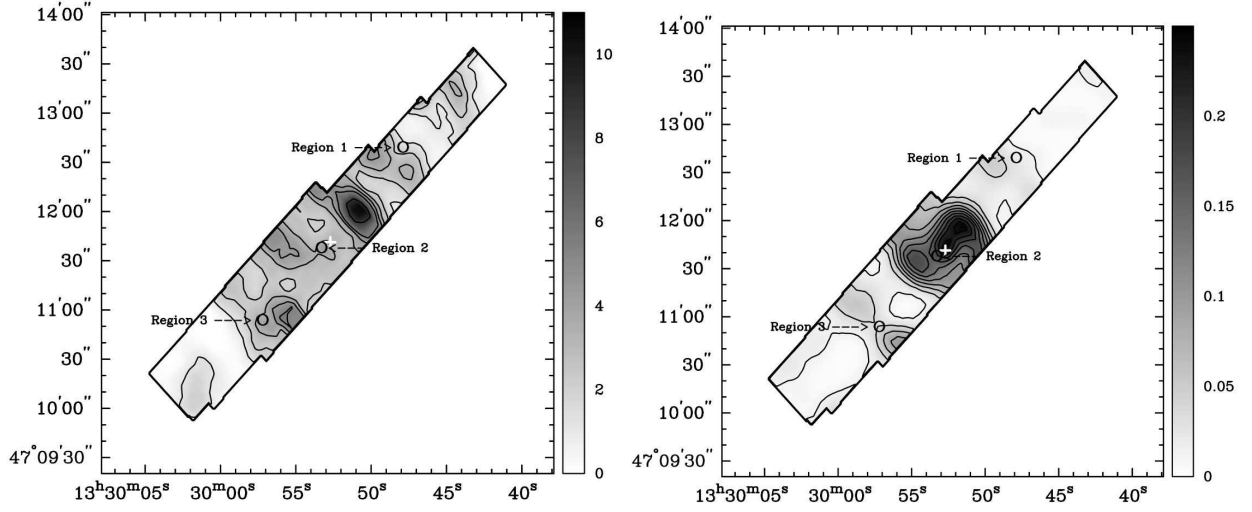


Fig. 3.— Shown are the warm ( $T = 100 - 300$  K)  $H_2$  (*left*) and hot ( $T = 400 - 1000$  K)  $H_2$  (*right*) surface density distributions. The surface density distributions are in units of  $M_{\odot} \text{ pc}^{-2}$ . Contours are overplotted for clarity. The warm  $H_2$  surface density contour levels are at 8.85, 5.55, 4.43, 3.32, 2.21, and 1.10  $M_{\odot} \text{ pc}^{-2}$ . The hot  $H_2$  contour levels are at 10 % of 0.25  $M_{\odot} \text{ pc}^{-2}$ . The hot  $H_2$  surface density distribution is derived from the fit to the  $H_2$  S(2) –  $H_2$  S(5) lines and the warm  $H_2$  surface density distribution is derived from the fit to the  $H_2$  S(0) –  $H_2$  S(2) lines, corrected for the contribution of the hot  $H_2$  phase. The three circles denote the regions of the excitation diagrams in Figure 2.

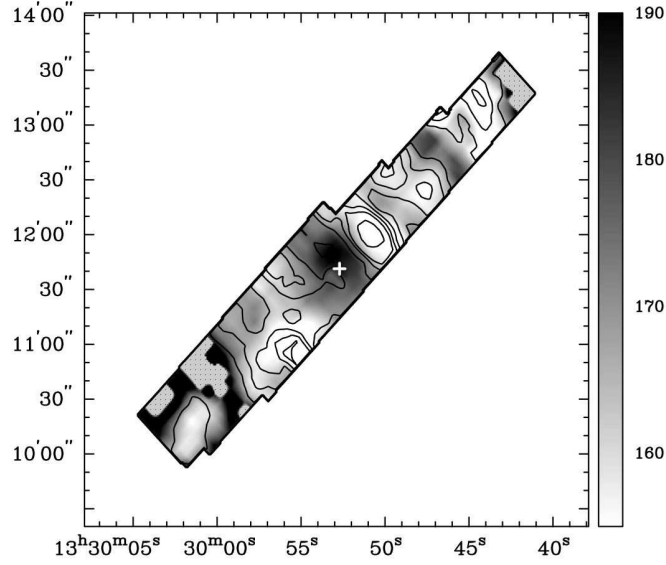


Fig. 4.— The warm ( $T = 100 - 300$  K)  $H_2$  surface density distribution (in contours) compared to the warm  $H_2$  temperature distribution (in grayscale, in units Kelvin). The warm  $H_2$  temperature and surface density distributions are derived from the fit to the excitation diagrams across the strip for the  $H_2$  S(0) –  $H_2$  S(2) lines, corrected for the contribution of the hot ( $T = 400 - 1000$  K)  $H_2$  phase. Surface density contour levels are at 8.85, 5.55, 4.43, 3.32, 2.21, and  $1.10 \text{ M}_\odot \text{ pc}^{-2}$  (same as in Figure 3). The non-rectangular shape to the map is due to the slight offset of the *Spitzer* IRS SL strip relative to the LL strip.

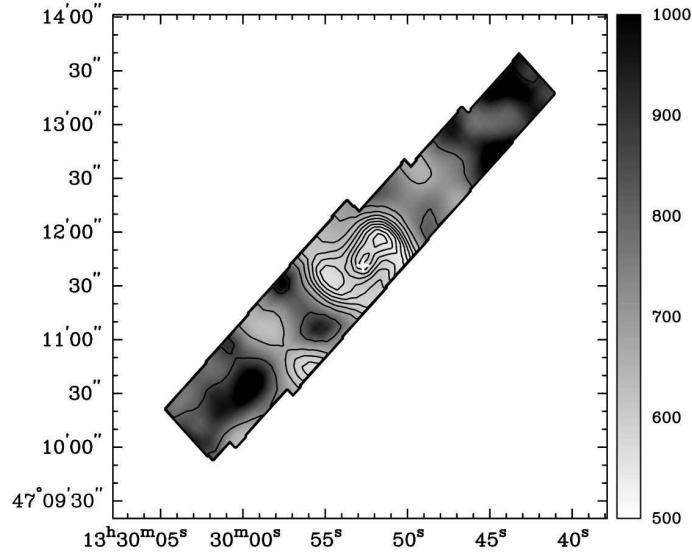


Fig. 5.— The hot ( $T = 400 - 1000$  K) H<sub>2</sub> surface density distribution (in contours) compared to the hot H<sub>2</sub> temperature distribution (in grayscale, in units Kelvin). The hot H<sub>2</sub> temperature and surface density distributions are derived from the fit to the excitation diagrams across the strip for the H<sub>2</sub> S(2) – H<sub>2</sub> S(5) lines. Surface density contour levels are at 10% of  $0.25 \text{ M}_{\odot} \text{ pc}^{-2}$  (same as in Figure 3).

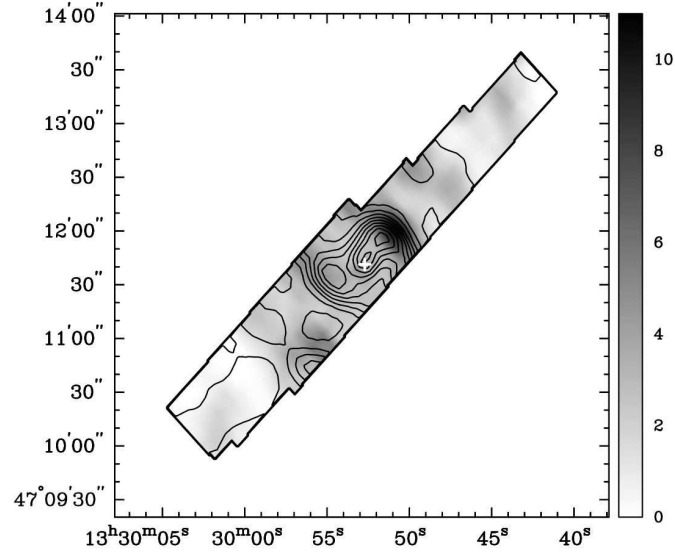


Fig. 6.— The warm ( $T = 100 - 300$  K)  $H_2$  surface density (in grayscale) compared to the hot ( $T = 400 - 1000$  K)  $H_2$  surface density (in contours). Contours levels for the hot  $H_2$  surface density distribution are at 10% of the maximum surface density  $0.25 M_\odot \text{ pc}^{-2}$ . The grayscale is in units of  $M_\odot \text{ pc}^{-2}$ .

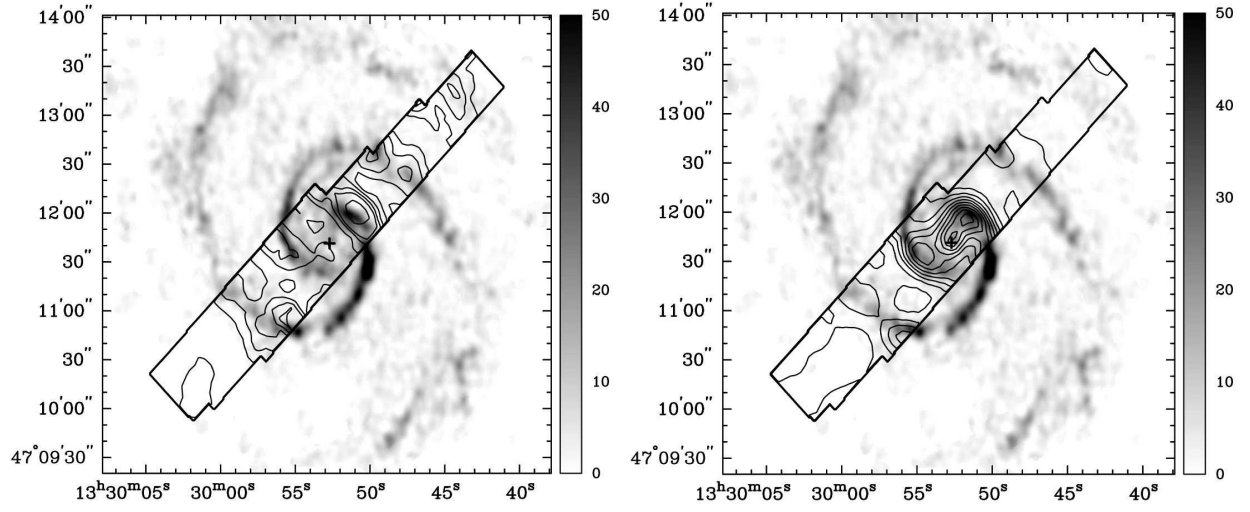


Fig. 7.— *Left*: Comparison of CO intensity (in grayscale) to the warm ( $T = 100 - 300$  K) H<sub>2</sub> surface density (in contours). The CO intensity is in units of Jy beam s<sup>-1</sup>. The warm H<sub>2</sub> surface density contours are the same as in Figures 3 and 4. *Right*: Comparison of CO intensity (in grayscale) to the hot ( $T = 400 - 1000$  K) H<sub>2</sub> surface density (in contours). The CO intensity is in units of Jy beam s<sup>-1</sup>. The hot H<sub>2</sub> surface density contours are the same as in Figures 3 and 5.

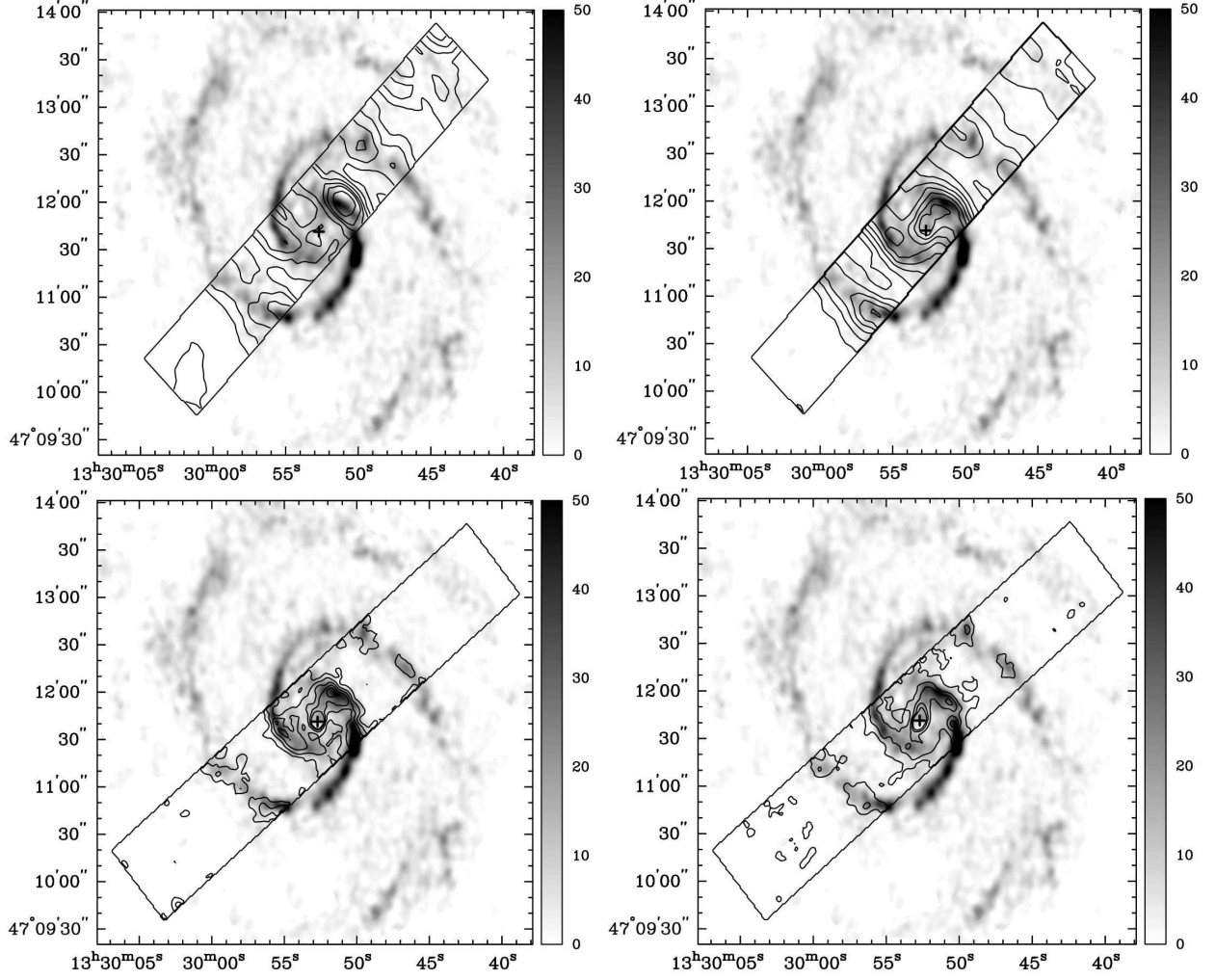


Fig. 8.— Comparison of the CO emission to the  $\text{H}_2$  S(0) (*top left*),  $\text{H}_2$  S(1) (*top right*),  $\text{H}_2$  S(2) (*bottom left*), and  $\text{H}_2$  S(3) (*bottom right*) emission. The CO emission maps are in units of  $\text{Jy beam s}^{-1}$ . Contour levels for  $\text{H}_2$  S(0),  $\text{H}_2$  S(1),  $\text{H}_2$  S(2), and  $\text{H}_2$  S(3) are the same as in Figure 1.

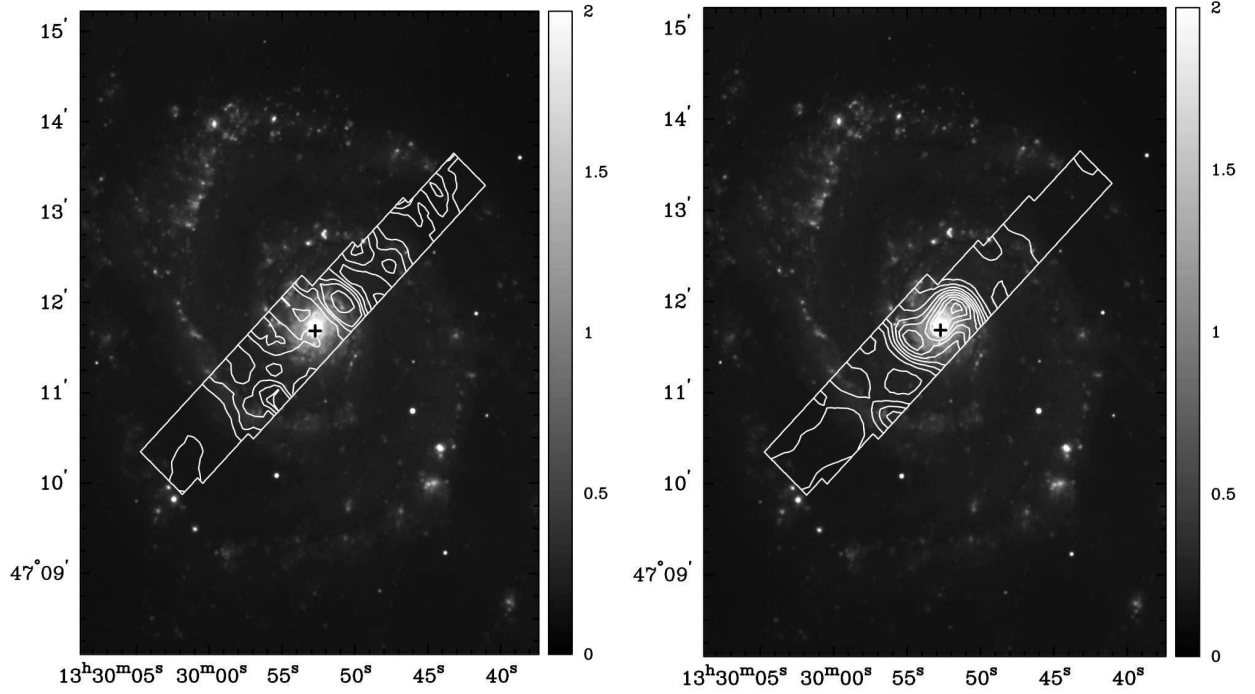


Fig. 9.— *Left*: Comparison of  $H\alpha$  (in grayscale) to the warm ( $T = 100 - 300$  K)  $H_2$  surface density (in contours). The  $H\alpha$  image is in units of counts  $s^{-1}$ . The warm  $H_2$  surface density contours are the same as in Figures 3 and 4. *Right*: Comparison of  $H\alpha$  (in grayscale) to the hot ( $T = 400 - 1000$  K)  $H_2$  surface density (in contours). The  $H\alpha$  image is in units of counts  $s^{-1}$ . The hot  $H_2$  surface density contours are the same as in Figures 3 and 5.

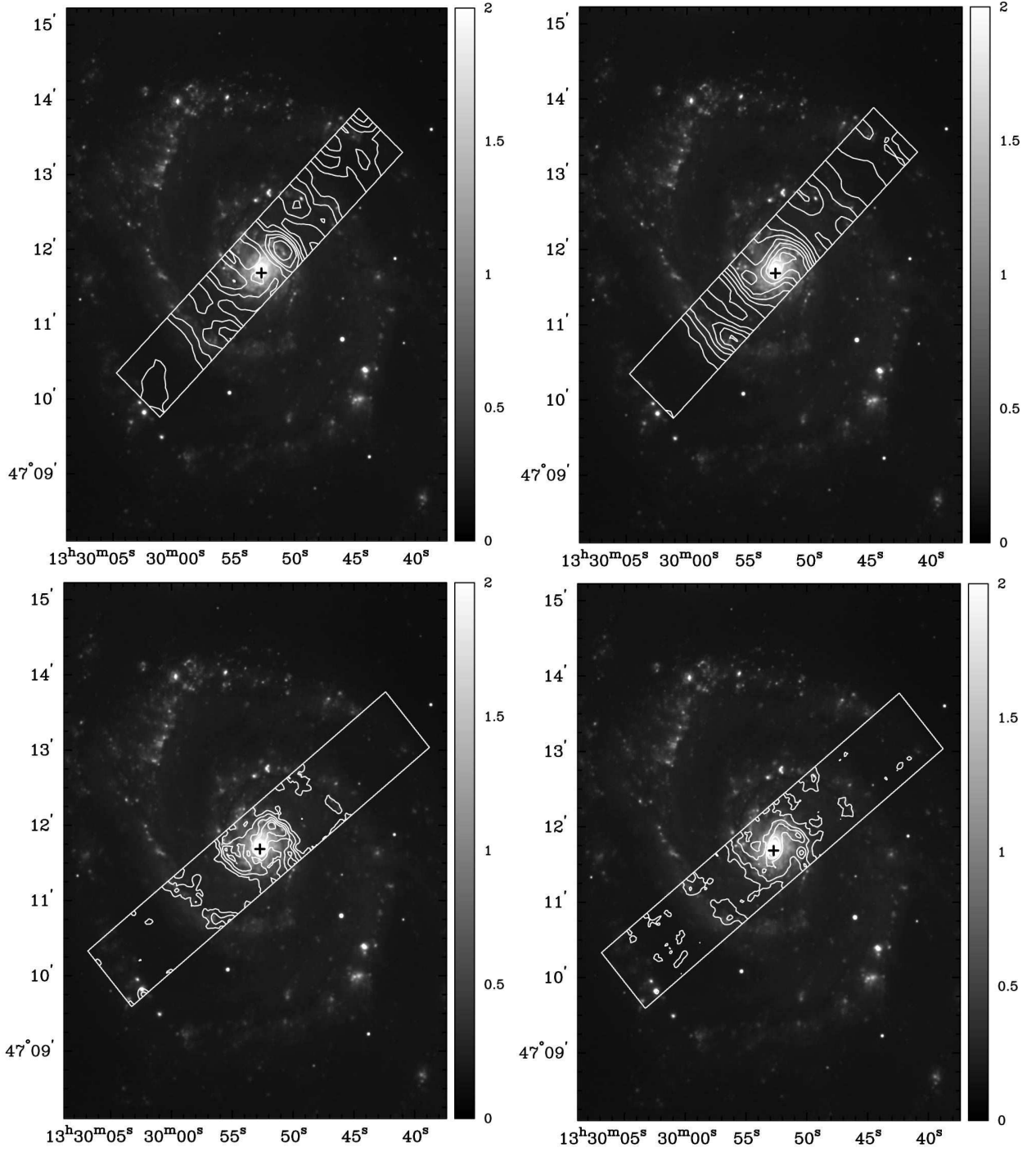


Fig. 10.— Comparison of  $H\alpha$  emission to the  $H_2$  S(0) (*top left*),  $H_2$  S(1) (*top right*),  $H_2$  S(2) (*bottom left*), and  $H_2$  S(3) (*bottom right*) emission. The  $H\alpha$  image is in units of counts  $s^{-1}$ . Contour levels for  $H_2$  S(0),  $H_2$  S(1),  $H_2$  S(2), and  $H_2$  S(3) are the same as in Figure 1.



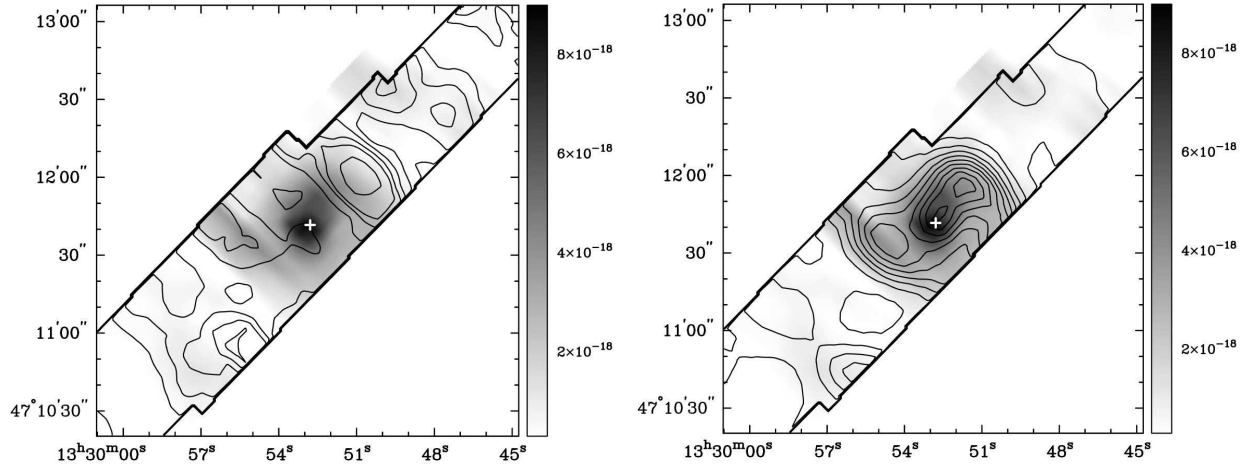


Fig. 11.— *Left*: Comparison of the [O IV](25.89  $\mu$ m) emission (in grayscale) to the warm ( $T = 100$  K - 300 K) H<sub>2</sub> surface density distribution (in contours). Hot H<sub>2</sub> surface density contours are the same as in Figures 3 and 4. *Right*: Comparison of the [O IV](25.89  $\mu$ m) emission (in grayscale) to the hot ( $T = 400$  - 1000 K) H<sub>2</sub> surface density distribution (in contours). Hot H<sub>2</sub> surface density contours are the same as in Figures 3 and 5. The [O IV](25.89  $\mu$ m) emission is in units of W m<sup>-2</sup>.

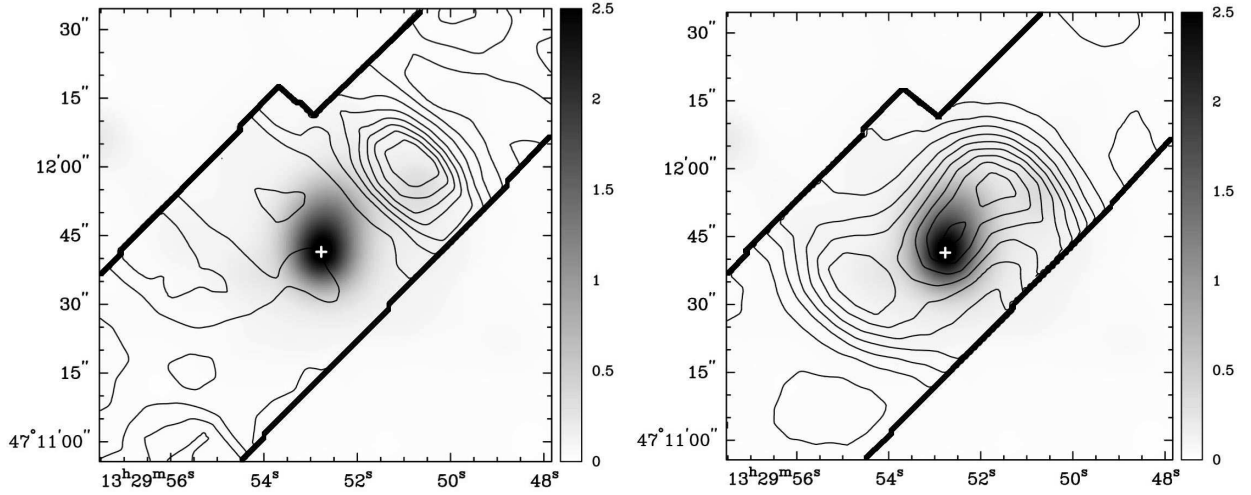


Fig. 12.— *Left*: Comparison of the smoothed 0.5 – 10 keV X-ray emission band (in grayscale) to the warm ( $T = 100 - 300$  K)  $\text{H}_2$  surface density distribution (in contours). The X-ray image has been smoothed to the same resolution as the warm  $\text{H}_2$  surface density map. X-ray emission is in units of counts.  $\text{H}_2$  surface density contours are the same as in Figures 3 and 4. *Right*: Comparison of the smoothed 0.5 – 10 keV X-ray emission band (in grayscale) to the hot ( $T = 400 - 1000$  K)  $\text{H}_2$  surface density distribution (in contours). The  $\text{H}_2$  surface density distribution contours are the same as in Figures 3 and 5.

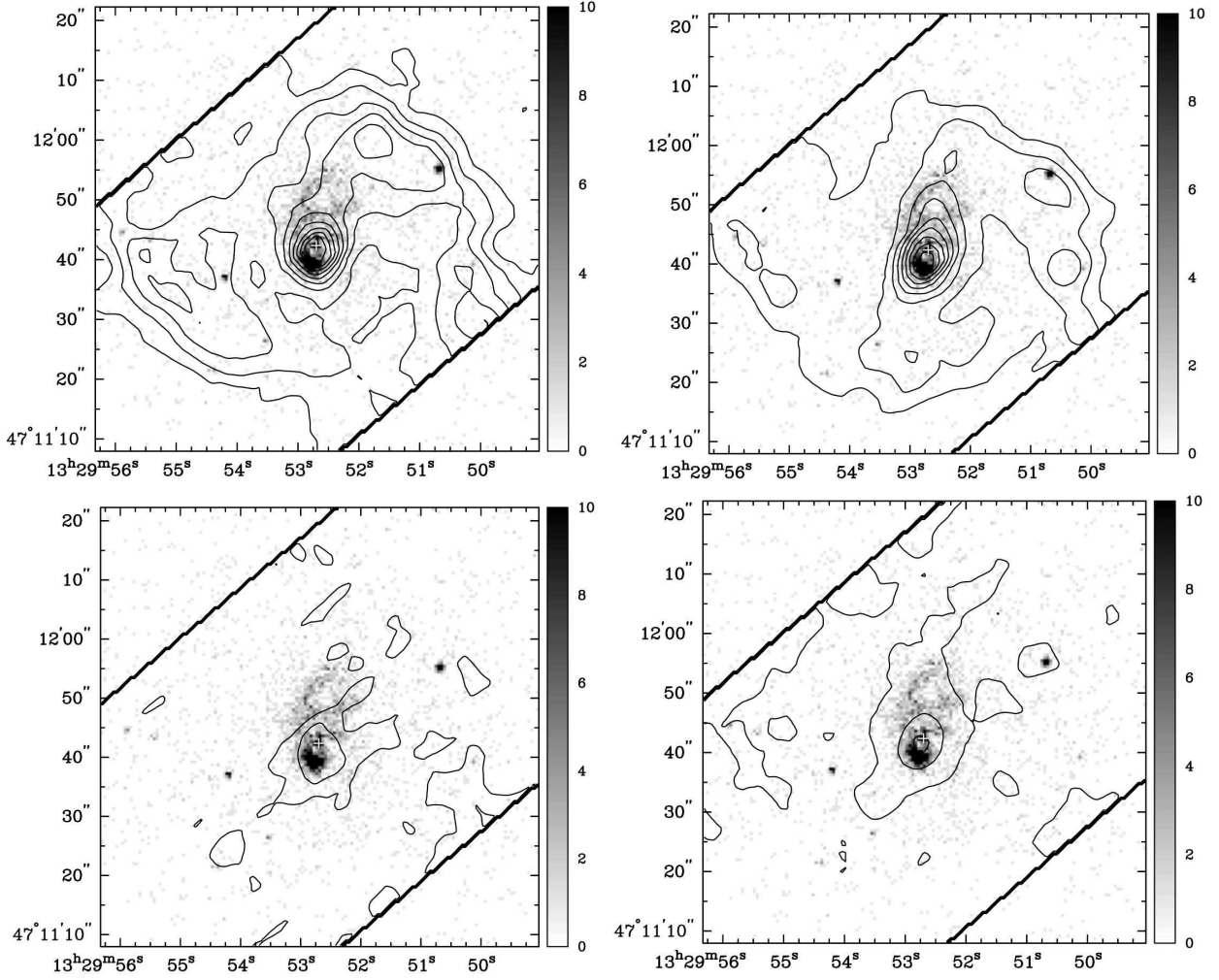


Fig. 13.— Comparison of the 0.5 – 10 keV X-ray emission band (in grayscale) to the H<sub>2</sub> S(2) (*top left*), H<sub>2</sub> S(3) (*top right*), H<sub>2</sub> S(4) (*bottom left*), and H<sub>2</sub> S(5) (*bottom right*) emission in the nuclear region of M51. X-ray emission is in units of counts. The H<sub>2</sub> S(2) and H<sub>2</sub> S(3) emission contours are at 10 % of their peak values ( $2.20 \times 10^{-18}$  and  $1.35 \times 10^{-17}$  W m<sup>-2</sup>, respectively). The H<sub>2</sub> S(4) contours are at  $2.0 \times 10^{-18}$  and  $1.0 \times 10^{-18}$  W m<sup>-2</sup> and the H<sub>2</sub> S(5) contours are at  $7.3 \times 10^{-18}$ ,  $4.0 \times 10^{-18}$ , and  $8.0 \times 10^{-19}$  W m<sup>-2</sup>.

Table 1. H<sub>2</sub> Parameters

Transition	Wavelength ( $\mu\text{m}$ )	Rotational State (J)	Energy (E/k)	A ( $\text{s}^{-1}$ )	Statistical Weight (g)
H <sub>2</sub> (0-0)S(0)	28.22	2	510	$2.94 \times 10^{-11}$	5
H <sub>2</sub> (0-0)S(1)	17.04	3	1015	$4.76 \times 10^{-10}$	21
H <sub>2</sub> (0-0)S(2)	12.28	4	1682	$2.76 \times 10^{-9}$	9
H <sub>2</sub> (0-0)S(3)	9.66	5	2504	$9.84 \times 10^{-9}$	33
H <sub>2</sub> (0-0)S(4)	8.03	6	3474	$2.64 \times 10^{-8}$	13
H <sub>2</sub> (0-0)S(5)	6.91	7	4586	$5.88 \times 10^{-8}$	45

Note. — The statistical weight (g) is  $(2J+1)(2I+1)$  where  $I$  equals 1 for odd J transitions (ortho transitions) and  $I$  equals 0 for even J transitions (para transitions).